JOURNAL OF GEOPHYSICAL RESEARCH, VOL. 115, D01106, doi:10.1029/2009JD012802, 2010

Climate simulations with a new air-sea turbulent flux parameterization in the National Center for Atmospheric Research Community Atmosphere Model (CAM3)

Junmei Ban,[1,2] Zhiqiu Gao,[1] and Donald H. Lenschow[3]

Received 7 July 2009; revised 26 September 2009; accepted 7 October 2009; published 8 January 2010.

[1] This study examines climate simulations with the National Center for Atmospheric Research Community Atmosphere Model version 3 (NCAR CAM3) using a new air-sea turbulent flux parameterization scheme. The current air-sea turbulent flux scheme in CAM3 consists of three basic bulk flux equations that are solved simultaneously by an iterative computational technique. We recently developed a new turbulent flux parameterization scheme where the Obukhov stability length is parameterized directly by using a bulk Richardson number, an aerodynamic roughness length, and a heat roughness length. Its advantages are that it (1) avoids the iterative process and thus increases the computational efficiency, (2) takes account of the difference between z_{0m} and z_{0h} and allows large z_{0m}/z_{0h}, and (3) preserves the accuracy of iteration. An offline test using Tropical Ocean–Global Atmosphere Coupled Ocean-Atmosphere Response Experiment (TOGA COARE) data shows that the original scheme overestimates the surface fluxes under very weak winds but the new scheme gives better results. Under identical initial and boundary conditions, the original CAM3 and CAM3 coupled with the new turbulent flux scheme are used to simulate the global distribution of air-sea surface turbulent fluxes, and precipitation. Comparisons of model outputs against the European Remote Sensing Satellites (ERS), the Objectively Analyzed air-sea Fluxes (OAFlux), and Climate Prediction Center (CPC) Merged Analysis of Precipitation (CMAP) show that: (1) the new scheme produces more realistic surface wind stress in the North Pacific and North Atlantic trade wind belts and wintertime extratropical storm track regions; (2) the latent heat flux in the Northern Hemisphere trade wind zones shows modest improvement in the new scheme, and the latent heat flux bias in the western boundary current region of the Gulf Stream is reduced; and (3) the simulated precipitation in the new scheme is closer to observation in the Asian monsoon region.

Citation: Ban, J., Z. Gao, and D. H. Lenschow (2010), Climate simulations with a new air-sea turbulent flux parameterization in the National Center for Atmospheric Research Community Atmosphere Model (CAM3), *J. Geophys. Res.*, *115*, D01106, doi:10.1029/2009JD012802.

1. Introduction

[2] Accurate and efficient calculations of the surface fluxes are essential to all scales of numerical simulations of the atmosphere [*Lee*, 1997]. Bulk algorithms on the basis of Monin-Obukhov similarity (hereafter MOS) theory are widely used in numerical models to estimate surface fluxes. Because fluxes estimated with a bulk algorithm depend on the transfer coefficients and the transfer coefficients depend on the stability, bulk algorithms rely on iterative solutions to the three basic (velocity, temperature, and humidity) bulk flux equations [*Grachev and Fairall*, 1997]. These equations contain logarithmic and transcendental functions, so iteration can be costly in CPU time in numerical simulations of regional atmospheric models. It is especially true for high-resolution global simulation, because the calculation is repeated at all surface grid cells and at all time steps. That is the reason considerable efforts were made to pursue approximate analytical (noniterative) formulas of the transfer coefficients. Initially, *Louis* [1979] and *Louis et al.* [1982] fitted a polynomial to the solutions of the equations mentioned above so that the value of $\zeta(\equiv z/L)$ is estimated from the bulk Richardson number Ri_B, which has been widely used in several numerical mesoscale models [e.g., *Ulrickson and Mass*, 1990; *Pielke et al.*, 1992]. However, just as *Wang et al.* [2002] pointed out, the most critical weakness of the Louis scheme is the assumption that $z_{0m} = z_{0h} = z_{0e}$, where z_{0m}, z_{0h}, and z_{0e} are roughness lengths for momentum, heat, and moisture, respectively. A variety of different fits are found in the literature, depending on the choices of wind speed dependencies of the neutral transfer coefficients and the em-

[1]State Key Laboratory of Atmospheric Boundary Layer Physics and Atmospheric Chemistry, Institute of Atmospheric Physics, Chinese Academy of Sciences, Beijing, China.
[2]Graduate University of Chinese Academy of Sciences, Beijing, China.
[3]Mesoscale and Meteorology Division, National Center for Atmospheric Research, Boulder, Colorado, USA.

0148-0227/10/2009JD012802$09.00

pirical MOS profile functions [e.g., *Byun*, 1990; *Launiainen*, 1995]. We recently developed a noniterative turbulent flux parameterization scheme (hereafter referred to as the GLL scheme (Z. Gao et al., An improved approach for turbulent transfer coefficients in the surface layer for numerical models, submitted to *Boundary-Layer Meteorology*, 2010)). The motivation is from *Louis et al.* [1982], *Launiainen* [1995], *Beljaars and Holtslag* [1991], and *Högström* [1996]. The GLL scheme uses two new polynomial equations by applying a multiple regression method to iterative results of the bulk algorithms.

[3] Persistent concerns regarding climate change prediction have led to increased scrutiny of potential sources of errors in model outputs. The bulk algorithm used in the National Center for Atmospheric Research (NCAR) Community Atmosphere Model version 3 overestimates the latent heat flux under very weak wind conditions [*Zeng et al.*, 1998; *Brunke et al.*, 2002, 2003]. The current CAM3 algorithm does two iterations in the flux calculation module, so a noniterative turbulent flux parameterization scheme that (1) not only takes account of the difference between z_{0m} and z_{0h}, but also allows large z_{0m}/z_{0h}, and (2) still preserves the accuracy of iteration would be a more efficient and accurate approach.

[4] The negative results of the directly tested turbulent flux parameterization scheme within CAM3 could be due to (1) specific properties of the atmosphere above the surface change in response to variations in surface fluxes, (2) the complication of isolating problems caused by deficiencies of the turbulent flux parameterization scheme from those caused by deficiencies in other parts of the models, and (3) the lack of high-resolution spatial and temporal observations. Therefore, the first objective of this study is to compare offline the turbulent flux parameterization scheme of CAM3 and the GLL scheme to the TOGA COARE flux measurements (http://seaflux.gfdi.fsu.edu/staticpages/index.php/valdata). The roughness length for momentum obtained by *Large and Pond* [1982] and the profile equations by *Dyer* [1974] are used in the air-sea flux scheme for CAM3.

[5] After demonstrating the success of the GLL scheme in the offline test, we replace the original turbulent flux scheme in CAM3 with the GLL scheme. The second objective of the present study is then to investigate whether the GLL scheme produces a realistic estimate of global precipitation.

2. Description of Models and Parameterizations

2.1. Brief Overview of the Community Atmosphere Model

[6] The Community Atmosphere Model (CAM) is designed to be a modular and versatile model suitable for a broad array of climate studies [*Collins et al.*, 2004]. It can be integrated with spectral Eulerian, semi-Lagrangian, or finite volume dynamics [*Collins et al.*, 2006a]. Comparable to the previous Community Climate Model (CCM) version 3, CAM3 can be run either as a stand-alone global climate model (GCM) or as a component of the Community Climate System Model (CCSM) [*Collins et al.*, 2006b]. In its stand-alone mode, CAM3 is integrated together with the Community Land Model (CLM) [*Bonan et al.*, 2002; *Oleson et al.*, 2004], a thermodynamic sea ice model, and a sea surface temperature (SST) product. The CAM3 fixes the SST and updates it to a value interpolated from monthly means read in from an external data set [*Rasch et al.*, 2006]. The most important difference between CAM3 and CCM3 is associated with changes to the parameterized physics package. A more detailed description of improvements in CAM3 is presented in a special issue on Community Climate System Model (CCSM) (*Journal of Climate, 19*(11), June 2006).

[7] In CAM3, air-sea turbulent fluxes are calculated from bulk formulas,

$$\begin{aligned} \tau &\equiv \rho_a u_*^2 = \rho_a C_M U^2, \\ H &\equiv \rho_a c_p u_* \theta_* = \rho_a c_p C_H U \Delta\theta, \\ L_e E &\equiv -L_e \rho_a u_* q_* = L_e \rho_a C_E U \Delta q, \end{aligned} \tag{1}$$

where τ, H, and L_eE are the turbulent momentum, sensible heat, and latent heat fluxes respectively; ρ_a is the atmospheric surface density; u_*, θ_*, and q_* are the friction velocity, potential temperature scaling parameter, and water vapor scaling parameter, respectively; C_M, C_H, and C_E are the turbulent momentum, heat, and moisture exchange coefficients, respectively; U is the horizontal wind speed; c_p is the specific heat; $\Delta\theta$ is the potential temperature difference between the sea surface and the lowest model level; L_e is the latent heat of evaporation; $\Delta q = q_s(T_s) - q_a$ is the specific humidity difference, where q_a is the specific humidity at the lowest model level, and $q_s(T_s)$ is the saturation specific humidity at the sea surface where the sea surface temperature is T_s. The exchange coefficients are

$$\begin{aligned} C_M &= k^2 \left[\ln\left(\frac{z_A}{z_{0m}}\right) - \psi_m \right]^{-2}, \\ C_H &= k^2 \left[\ln\left(\frac{z_A}{z_{0m}}\right) - \psi_m \right]^{-1} \left[\ln\left(\frac{z_A}{z_{0h}}\right) - \psi_h \right]^{-1}, \\ C_E &= k^2 \left[\ln\left(\frac{z_A}{z_{0m}}\right) - \psi_m \right]^{-1} \left[\ln\left(\frac{z_A}{z_{0e}}\right) - \psi_e \right]^{-1}, \end{aligned} \tag{2}$$

where k(= 0.4) is the von Karman's constant, z_A is the height over the sea surface, and (following *Dyer* [1974]) ψ_m, ψ_h, and ψ_e are the integrated flux profiles for momentum, sensible heat, and latent heat.

[8] Under stable conditions ($\zeta > 0$),

$$\psi_m(\zeta) = -\beta_m \zeta, \psi_h(\zeta) = -\beta_h \zeta / R, \tag{3}$$

where $\beta_m = \beta_h = 5$, $R = 1$. Under unstable conditions ($\zeta < 0$),

$$\begin{aligned} \psi_m(\zeta) &= 2\ln\left(\frac{1+\chi}{2}\right) + \ln\left(\frac{1+\chi^2}{2}\right) - 2\tan^{-1}\chi + \frac{\pi}{2}, \\ \chi &= (1 - \gamma_m \zeta)^{1/4} \end{aligned} \tag{4}$$

and

$$\psi_h(\zeta) = \psi_e(\zeta) = 2\ln\left(\frac{1+y^2}{2}\right), y = R(1 - \gamma_h \zeta)^{1/2}, \tag{5}$$

where $\gamma_m = \gamma_h = 16$, $R = 1$, and the stability parameter

$$\zeta \equiv \frac{z}{L} = \frac{kgz}{u_*^2}\left(\frac{\theta_*}{\theta_v} + \frac{q_*}{\varepsilon^{-1} + q_a}\right), \tag{6}$$

where g is the gravitational acceleration, θ_ν is the virtual potential temperature, and $\varepsilon = 0.606$.

[9] Over the ocean, the roughness length for moisture $z_{0e} = 9.5 \times 10^{-5}$ m under all conditions, and the roughness length for heat $z_{0h} = 2.2 \times 10^{-9}$ m for $\zeta > 0$, and $z_{0h} = 4.9 \times 10^{-5}$ m for $\zeta \leq 0$ [*Large and Pond*, 1982]. The momentum roughness length is estimated from the 10 m wind speed, i.e.,

$$z_{0m} = 10 \exp\left[-kC_{10N}^{-1}\right], \tag{7}$$

where C_{10N} is the neutral drag coefficient at 10 m height, which is given by *Large et al.* [1994] as $C_{10N} = c_4 U_{10}^{-1} + c_5 + c_6 U_{10}$, where $c_4 = 2.70 \times 10^{-3}$, $c_5 = 1.42 \times 10^{-4}$, $c_6 = 7.64 \times 10^{-5}$, and U_{10} is the wind speed at 10 m height.

[10] Since equations (1)–(6) include u_*, θ_*, q_*, and ζ, which must adjust to each other, an iterative computational method is used to solve the whole system simultaneously at the first grid level in CAM3.

2.2. Brief Description of the GLL Scheme

[11] For the stable region, we use the scheme suggested by *Beljaars and Holtslag* [1991],

$$\psi_m = -a\zeta - b(\zeta - c/d)\exp(-d\zeta) - bc/d, \tag{3'}$$

$$\psi_h = \psi_q = -(1 + 2a\zeta/3)^{2/3} - b(\zeta - c/d)\exp(-d\zeta) - bc/d + 1, \tag{3''}$$

where $a = 1$, $b = 0.667$, $c = 5$, $d = 0.35$, and

$$\zeta = ((a_{11}\ln(z_0/z_{0h}) + a_{12})\ln(z/z_0) + a_{21}\ln(z_0/z_{0h}) + a_{22})Ri_B^2 + ((b_{11}\ln(z_0/z_{0h}) + b_{12})\ln(z/z_0) + b_{21}\ln(z_0/z_{0h}) + b_{22})Ri_B, \tag{6'}$$

where $a_{11} = 0.0593$, $a_{12} = -0.237$, $a_{21} = -5.639$, $a_{22} = 49.269$, $b_{11} = -0.067$, $b_{12} = 1.471$, $b_{21} = -0.390$, and $b_{22} = -3.605$.

[12] For the unstable region, the formulas are the same as the original CAM3 (equations (4) and (5)), except that we use the values suggested by *Högström* [1996], $R = 0.95$, $\chi_m = 19$, $\gamma_h = 11.6$.

[13] The stability parameter ζ is

$$\zeta = ((b_{11}\ln(z_0/z_{0h}) + b_{12})\ln^2(z/z_0) + (b_{21}\ln(z_0/z_{0h}) + b_{22}) \cdot \ln(z/z_0) + b_{31}\ln^2(z_0/z_{0h}) + b_{32}\ln(z_0/z_{0h}) + b_{33})Ri_B, \tag{6''}$$

with $b_{11} = 0.0034$, $b_{12} = 0.004$, $b_{21} = -0.091$, $b_{22} = 0.872$, $b_{31} = 0.156$, $b_{32} = -0.908$, and $b_{33} = 0.161$. Equations (6') and (6'') are obtained by applying regression methods to the iteration results.

[14] The roughness lengths for momentum, heat, and moisture are based on COARE3.0 [*Fairall et al.*, 1996, 2003]: $z_0 = \frac{z_{ch}u_*^2}{g} + 0.11\frac{\nu}{u_*}$, where z_{ch} is the Charnock constant, ν is the kinematic viscosity, and

$$z_{ch} = \begin{cases} 0.011 & U \leq 10\,\mathrm{m\,s^{-1}} \\ 0.011 + \frac{0.007(U-10)}{8} & 10\,\mathrm{m/s} < U \leq 18\,\mathrm{m\,s^{-1}} \\ 0.018 & U > 18\,\mathrm{m\,s^{-1}} \end{cases}.$$

[15] The scalar roughness length is parameterized in terms of the roughness Reynolds number $R_r = z_{0m}u_*/\nu$ [*Liu et al.*, 1979], $z_{0h} = z_{0e} = \min(1.1 \times 10^{-4}, 5.5 \times 10^{-5}R_r^{-0.6})$.

2.3. Measured Data used for Offline Test

[16] The data used for evaluating offline the GLL scheme are from the National Oceanic and Atmospheric Administration (NOAA)/Environmental Technology Laboratory (ETL) research ships during TOGA COARE. ETL's seagoing flux system was deployed onboard the R/V *Moana Wave*. The ship was nominally positioned at 1.7°S and 156°E during three periods: 11 November to 3 December 1992, 17 December 1992 to 11 January 1993, and 28 January to 16 February 1993. The measurement system is described in detail by *Fairall et al.* [1997]. The hourly turbulent fluxes used herein are those derived from the covariance (or eddy correlation) and inertial dissipation (ID) methods. The latent and sensible heat fluxes determined from covariances are in general more reliable than the inertial dissipation fluxes [*Fairall et al.*, 1996] and hence are used here. Since the covariance wind stress data are less reliable mainly because of the difficulty in removing ship motion from the horizontal wind components, we use the ID wind stresses. Several vigorous rejection criteria have been used to avoid flow distortion and contamination of turbulence data, such as relative wind direction within 30° of the bow, no ship maneuvers and the ship not under way at full speed, no sea salt, rain, or sun contamination, and flow tilt within 10°. This reduced the total number of acceptable flux estimates to 527. Detailed information about the flux measurements is given by *Zeng et al.* [1998], *Fairall et al.* [2003], and *Brunke et al.* [2003].

2.4. Measured Data Used for CAM3 Evaluations

[17] Monthly mean sea level pressure (SLP) is used from National Centers for Environmental Prediction (NCEP) reanalysis2 for the period 1979–2008: ftp://ftp.cdc.noaa.gov/pub/Datasets/ncep.reanalysis2.derived/surface/. Monthly wind stresses from European Remote Sensing Satellites (ERS) are used as a proxy for observations in the present study, which were obtained through the Community Climate System Model, Atmospheric Model Working Group (CCSM AMWG): http://www.cgd.ucar.edu/cms/rneale/tools/amwg_mean_diagnostics.html. This data set is on a 2.8° × 2.8° grid from 1992 to 2000. Objectively analyzed air-sea fluxes (OAFlux) for the global oceans [*Yu et al.*, 2004] provide the 1° gridded surface turbulent heat fluxes for the period 1958–2006: http://oaflux.whoi.edu/data.html. The OAFlux product is different from other flux products in that it is not constructed from a single data source, but rather it is determined by objectively blending data from satellite and numerical weather prediction (NWP) model outputs while using in situ observations to assign the weights [*Yu et al.*, 2004; *Yu and Weller*, 2007]. This study uses Climate Prediction Center (CPC) Merged Analysis of Precipitation (CMAP) [*Xie and Arkin*, 1997] as a proxy for observations, which is a global monthly precipitation data set constructed from satellite estimates, gauge observations, and numerical model outputs. The data are online at ftp://ftp.cdc.noaa.gov/pub/Datasets/cmap/enh.

3. Results and Discussion

3.1. Offline Test

[18] Figure 1 shows the mean time series of wind speed, wind direction, air temperature at 15 m height (T_a) sea surface temperature (T_s), specific humidity at 15 m height (q_a) and at

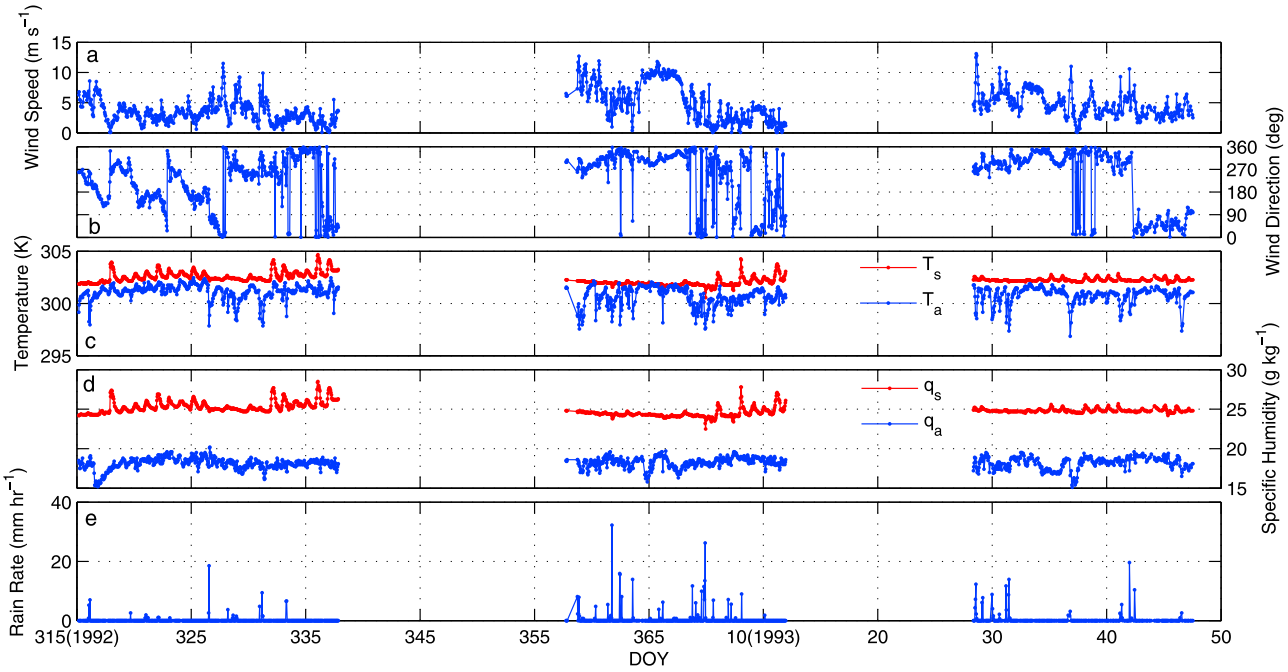

Figure 1. Time series from the R/V *Moana Wave* during TOGA COARE (at 1.7°S and 156°E) of (a) mean wind speed (m s^{-1}), (b) wind direction (degrees), (c) mean air temperature and sea surface temperature (K), (d) mean air specific humidity and sea surface specific humidity (g kg^{-1}), and (e) hourly precipitation (mm h^{-1}).

sea surface (q_s), and hourly precipitation obtained during the three periods of TOGA COARE and used here for the offline test. The observations were obtained during wintertime, with moderate wind speeds of 0–10 m s^{-1} (Figure 1a), and with mainly northwesterly wind direction (Figure 1b). Sea surface temperature is higher than air temperature, and the difference between them is less than 4 K (Figure 1c), i.e., the atmosphere is mainly unstably stratified. The scatter comparisons of (1) wind stress, (2) sensible heat flux, and (3) latent heat flux simulated by using the flux subroutine of the original CAM3 and by using the GLL scheme versus measurements are given in Figure 2. Figure 2 shows that CAM3 tends to overestimate the fluxes under weak wind conditions. The mean wind stress, sensible heat flux, and latent heat flux are 0.011 N m^{-2}, 5.43 W m^{-2}, and 72.34 W m^{-2}; the flux subroutine of the original CAM3 overestimates wind stress, sensible heat flux, and latent heat flux by 0.002 N m^{-2}, 2.43 W m^{-2}, and 11.28 W m^{-2}; and the GLL scheme realistically estimates wind stress and overestimates sensible heat flux and latent heat flux by 1.11 W m^{-2} and 6.49 W m^{-2}, respectively, under weak wind conditions (wind speed $<$ 4 m s^{-1}). With increased wind speed, CAM3 overestimates the sensible and latent heat fluxes, but underestimates the momentum flux. This bias is reduced in the GLL scheme, and the slope of the GLL scheme is closer to one than CAM3. Figure 3 shows the probability distribution functions (PDF) of the difference of (1) wind stress, (2) sensible heat flux, and (3) latent heat flux simulated by using the flux subroutine of the original CAM3 and by using the GLL scheme from the measurements. Compared to Figure 3a, the distributed data points of the wind stress difference tend to cluster in a narrower range centered by zero in Figure 3b. Comparison of Figures 3c and 3e against Figures 3d and 3f shows that the GLL scheme decreases the bias in sensible and latent heat fluxes respectively. Figures 2 and 3 show that the GLL scheme gives a better estimate of all the turbulent fluxes than the flux subroutine of the original CAM3.

[19] *Zeng et al.* [1998] found that the CAM3 overestimated latent heat flux under very weak wind conditions, and noted that under weak wind conditions, the computation of surface fluxes is strongly dependent upon both the treatment of free convection in the turbulence scheme and on the equations chosen for roughness lengths. The latent heat flux overestimate from CAM3 is primarily caused by the direct extrapolation of the neutral drag coefficient at 10 m height to convective conditions. We show in Figures 2 and 3 that the flux subroutine of the original CAM3 systematically overestimates all turbulent fluxes, and that the GLL scheme obviously helps CAM3 reduce the biases.

3.2. CAM3 Evaluations

[20] The simulations shown here are obtained with Eulerian dynamics at T42 spectral resolution (2.8° × 2.8°). The vertical hybrid coordinate is discretized to 26 levels extending from the surface to approximately 2 hPa. A climatological annual cycle of SST is used so that every year has the same annual cycle of SST. Two versions of CAM3 are presented here: the unaltered version (control) and the version utilizing the GLL scheme (CAM3_GLL). Both model versions are run for 15 years, and the monthly average values are produced. The monthly outputs for January and July are analyzed here.

3.2.1. Sea Level Pressure

[21] Figure 4 shows the sea level pressure (SLP) pattern from the NCEP, control run, and CAM3_GLL over the Northern Hemisphere during boreal winter. Figure 4b shows that the Aleutian low in the control run does not extend as far eastward and southward as NCEP (see Figure 4a). This

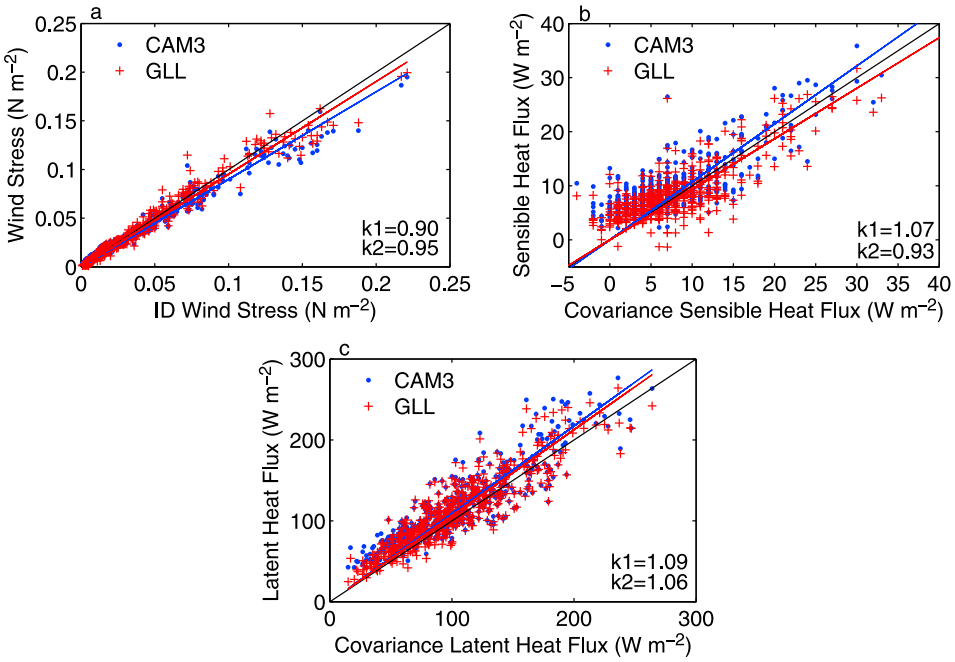

Figure 2. Fluxes calculated with the flux subroutine of the original CAM3 and by the GLL scheme versus measurements: (a) ID wind stress, (b) covariance sensible heat flux, and (c) covariance latent heat flux. The red and blue lines represent regression lines; k_1 and k_2 are the slopes of fluxes calculated by CAM3 and GLL versus measurement.

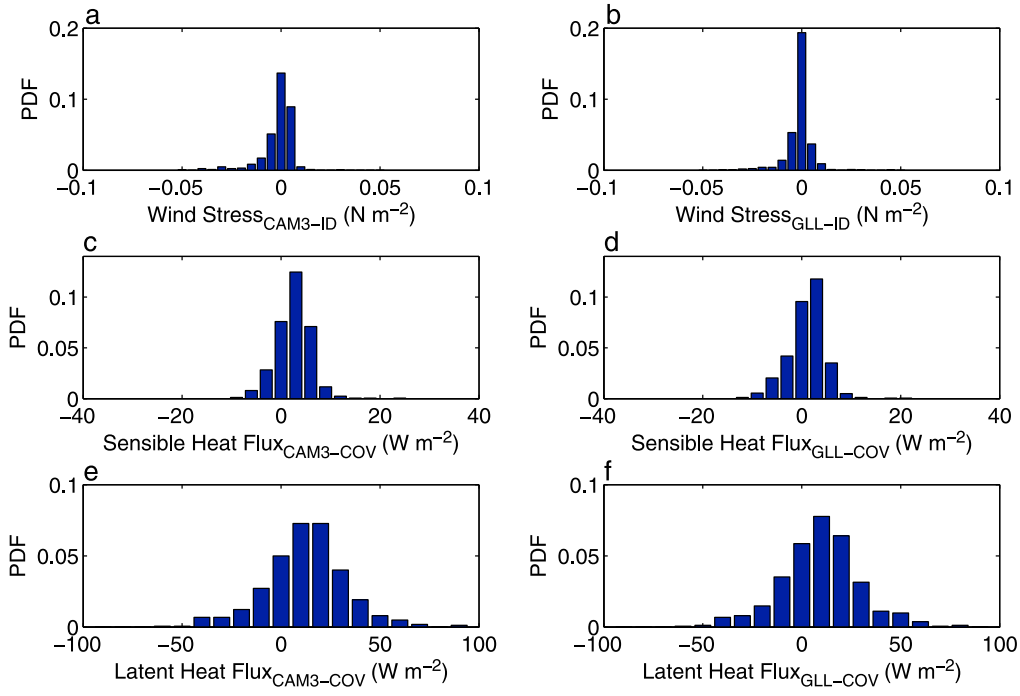

Figure 3. Probability distribution functions (PDF) of the difference between calculated fluxes (by using the flux subroutine of (left) the original CAM3 and (right) the GLL scheme) and measurements. (a and b) ID wind stress, (c and d) covariance sensible heat flux, and (e and f) covariance latent heat flux.

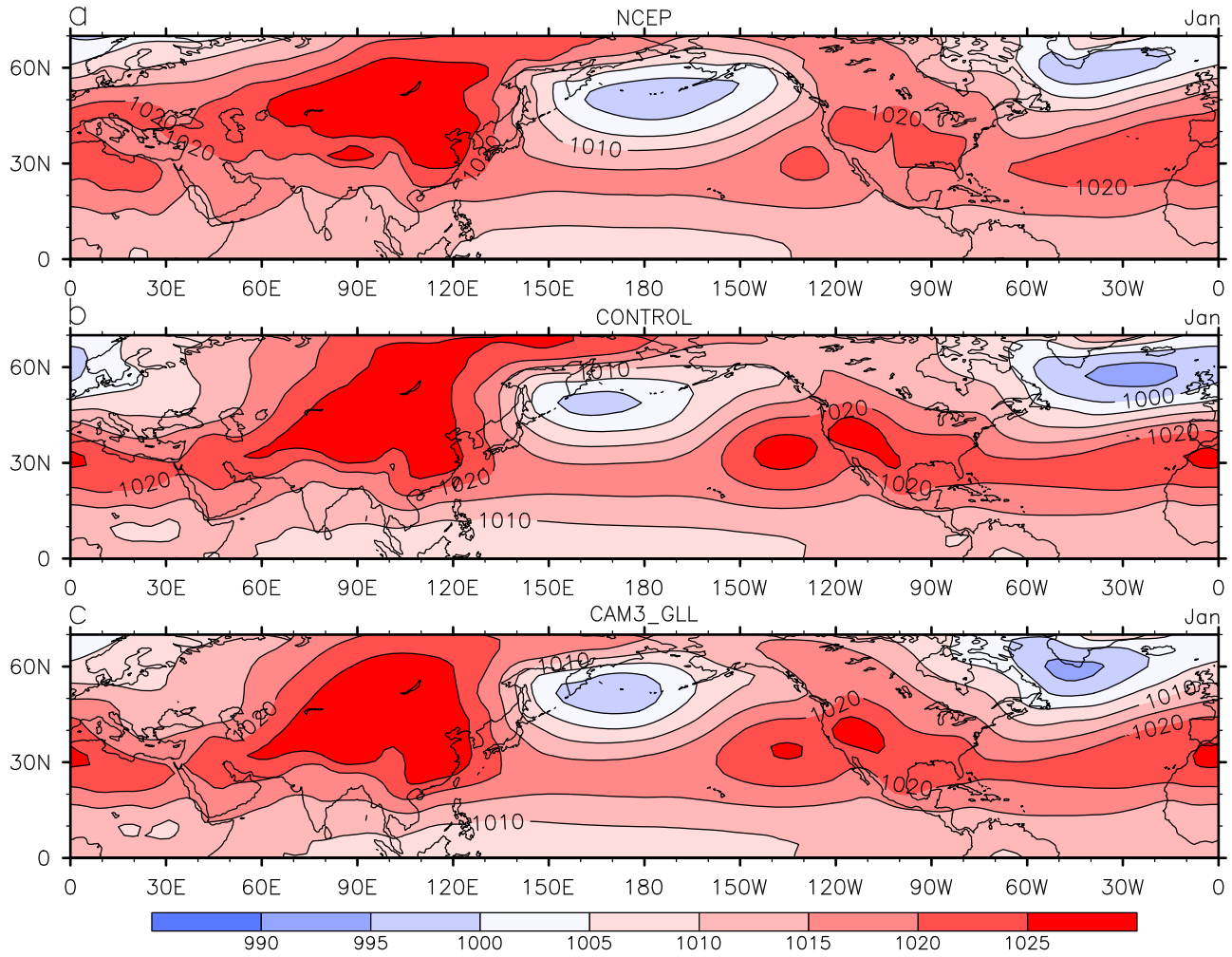

Figure 4. Sea level pressure (in hPa) in January. (a) NCEP (1979–2008) climatology, (b) control, and (c) CAM3_GLL.

regional bias is not evident in CCSM3 [*Hurrell et al.*, 2006], and *Alexander et al.* [2006] pointed out that this perhaps reflects the importance of interactive SST effects over this region. With the implementation of the GLL scheme, this bias is also alleviated, as Figure 4c shows that the Aleutian low is intensified, and the low-pressure center lies a few degrees longitude farther eastward. Additionally, the subtropical belt of high pressure over the Pacific in the control run is too strong, and CAM3_GLL produced a more realistic pattern in this region.

3.2.2. Surface Wind Stress

[22] The surface wind stress is an important parameter for coupling GCMs to dynamical ocean models, by which the atmospheric winds drive the oceanic currents, and the ocean acts as a sink for atmospheric momentum [*Trenberth*, 1990]. The main differences between ERS and control runs generally occur in two regions: the first is the subtropical trade winds over the Northern Hemisphere and the second is the storm track over the Southern Hemisphere. Figures 5–7 focus on these regions, and the statistical significance of CAM3_GLL and control run biases is tested by applying the Student's *t* test (95% level of significance).

[23] Figure 5b shows that the main bias in CAM3 relative to ERS is that the subtropical trade winds in CAM3 are too strong. This bias is consistent with higher sea level pressure than that observed throughout the subtropics during both seasons, as also reported previously by *Hurrell et al.* [2006]. CAM3_GLL reduces the bias of the subtropical belt of high pressure during boreal winter over the Pacific Ocean; thus it produces a more realistic simulation of the surface wind stress in the subtropical Pacific trades (see Figure 5c).

[24] Figures 6 and 7 focus on the surface wind stress in the storm track over Southern Hemisphere. The surface stress in the control run is much too large relative to satellite retrievals in the storm tracks (see Figures 6b and 7b), and the biases are linked to the simulated SLP. Large Southern Hemisphere winter SLP biases are found throughout the circumpolar region south of 50°S [*Hurrell et al.*, 2006], and the excessive meridional pressure gradient contributes to enhanced westerlies [*Capps and Zender*, 2008]. Although CAM3_GLL continues to share the same biases in this region, their magnitude is much reduced compared to the control run as seen in Figures 6c and 7c, and there is a statistically significant (at the 95% level) decrease in part of the region.

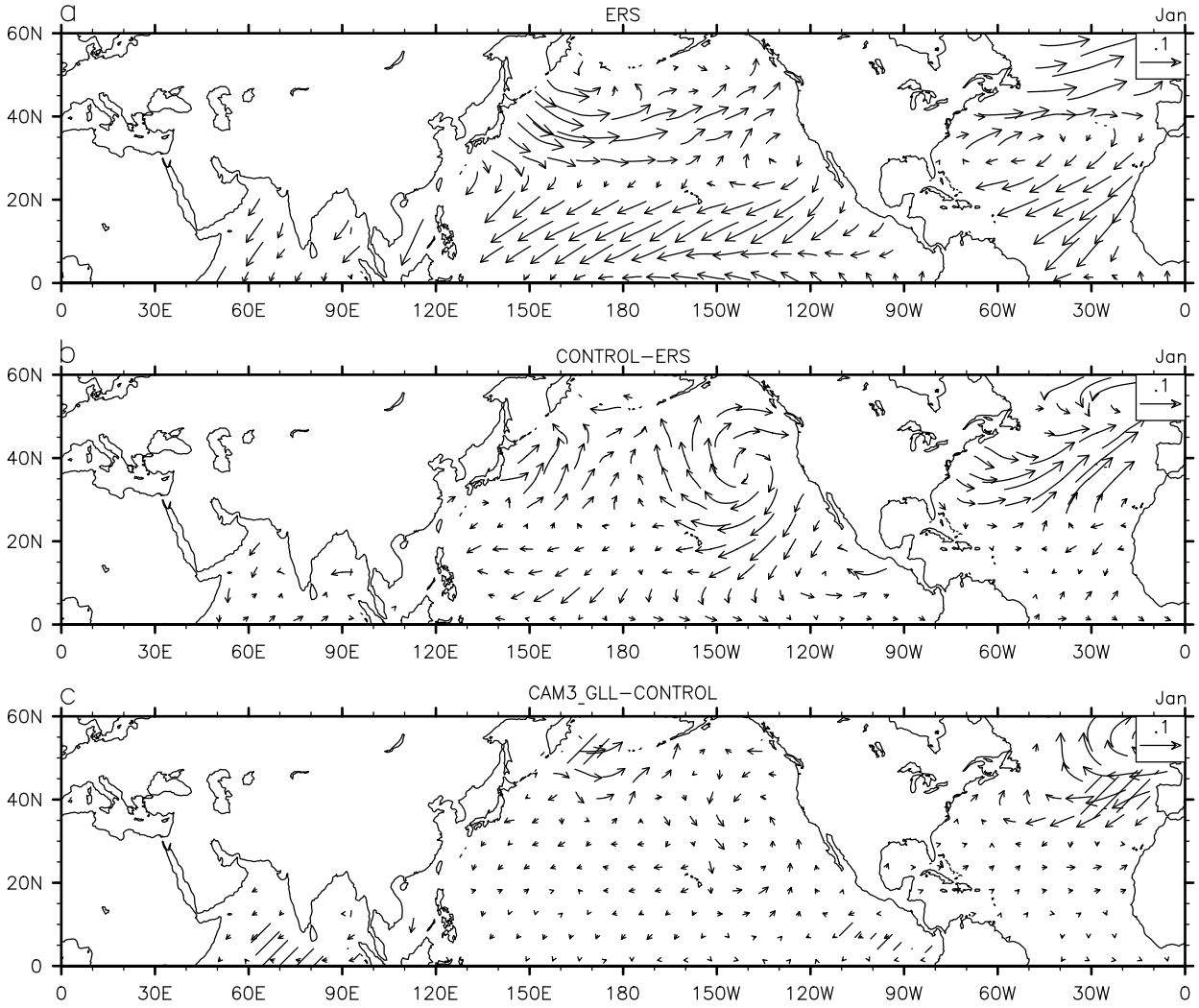

Figure 5. Surface wind stress vectors (in N m^{-2}) over the Northern Hemisphere in January. (a) ERS (1992–2000) climatology, (b) the difference between the control run and ERS, and (c) the difference between CAM3_GLL and the control run. Shaded areas show significant change at the 95% level, estimated by a Student's *t* test.

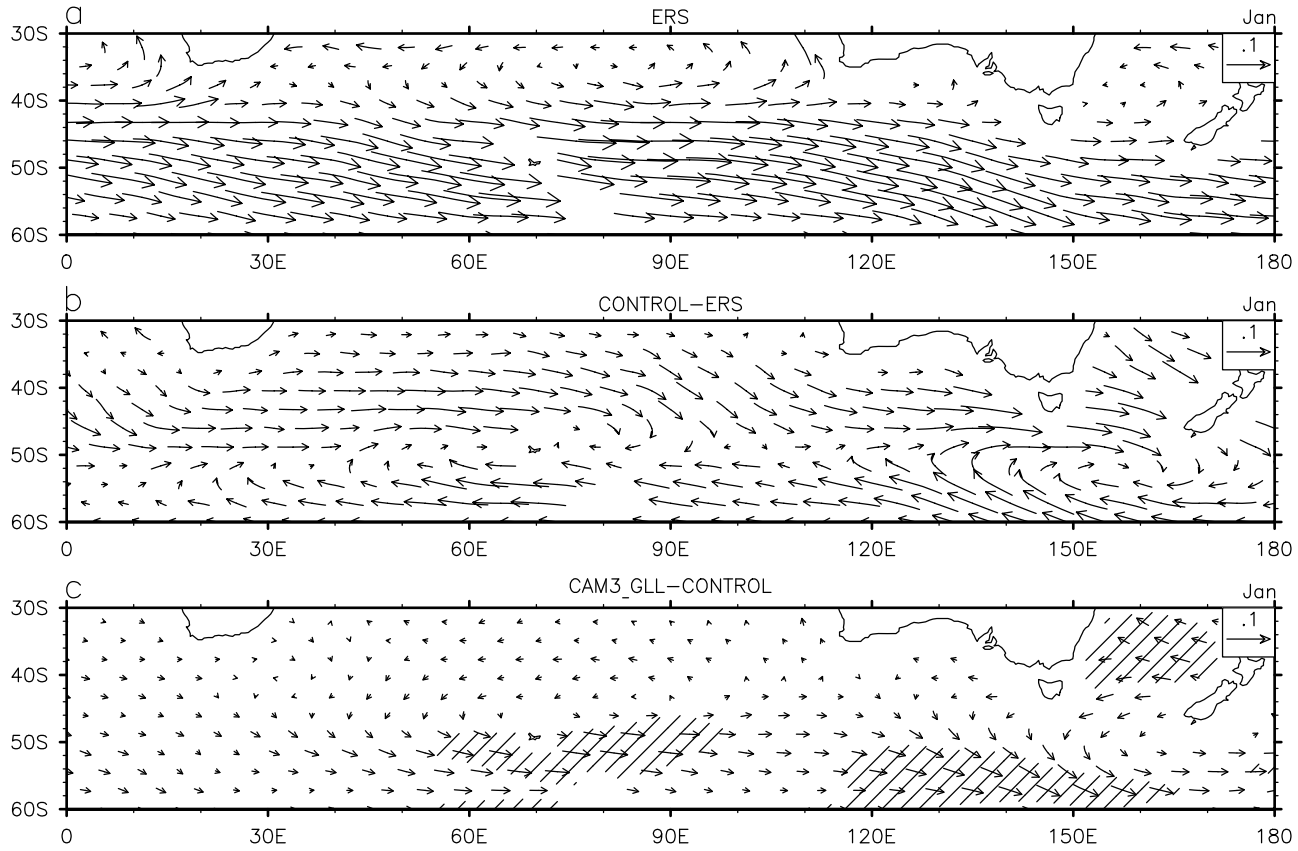

Figure 6. Surface wind stress vectors (in N m^{-2}) over 30°S–60°S in January. (a) ERS (1992–2000) climatology, (b) the difference between the control run and ERS, and (c) the difference between CAM3_GLL and the control run. Shaded areas show significant change at the 95% level, estimated by a Student's *t* test.

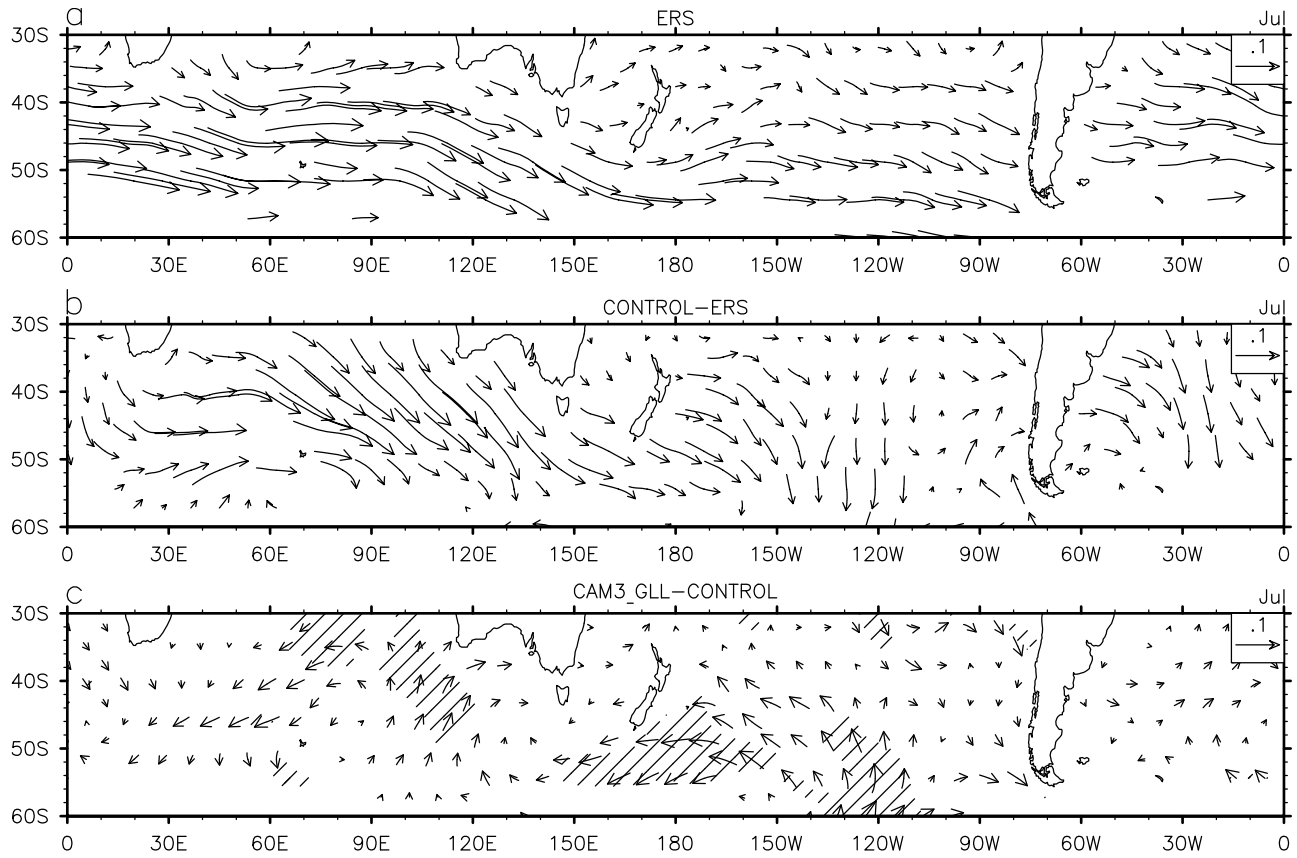

Figure 7. Same as Figure 6 but for July.

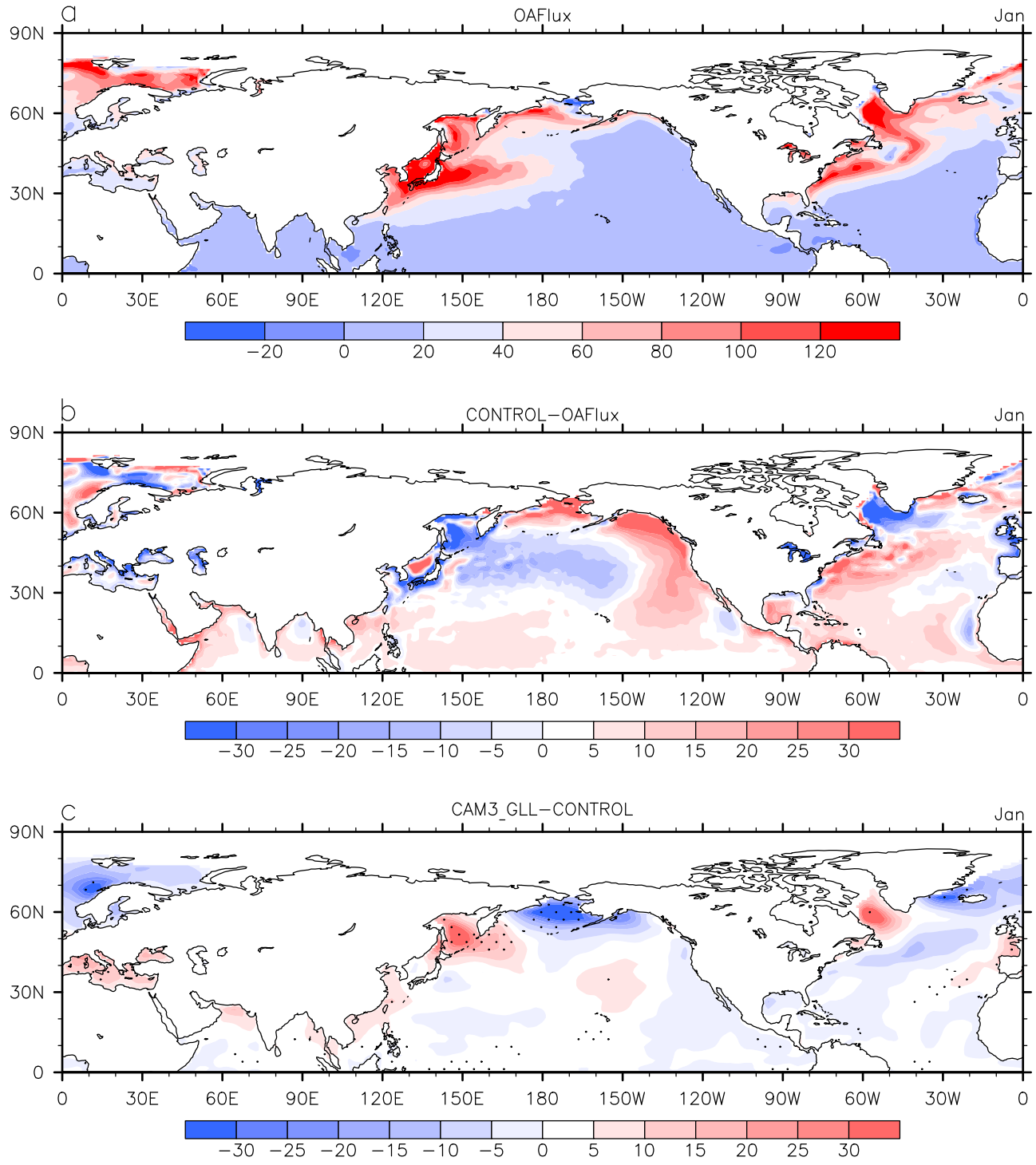

Figure 8. Surface sensible heat flux (in W m^{-2}) in January. (a) OAFlux (1958–2006), (b) the difference between the control run and OAFlux, and (c) the difference between CAM3_GLL and the control run. Shaded areas show significant change at the 95% level, estimated by a Student's *t* test.

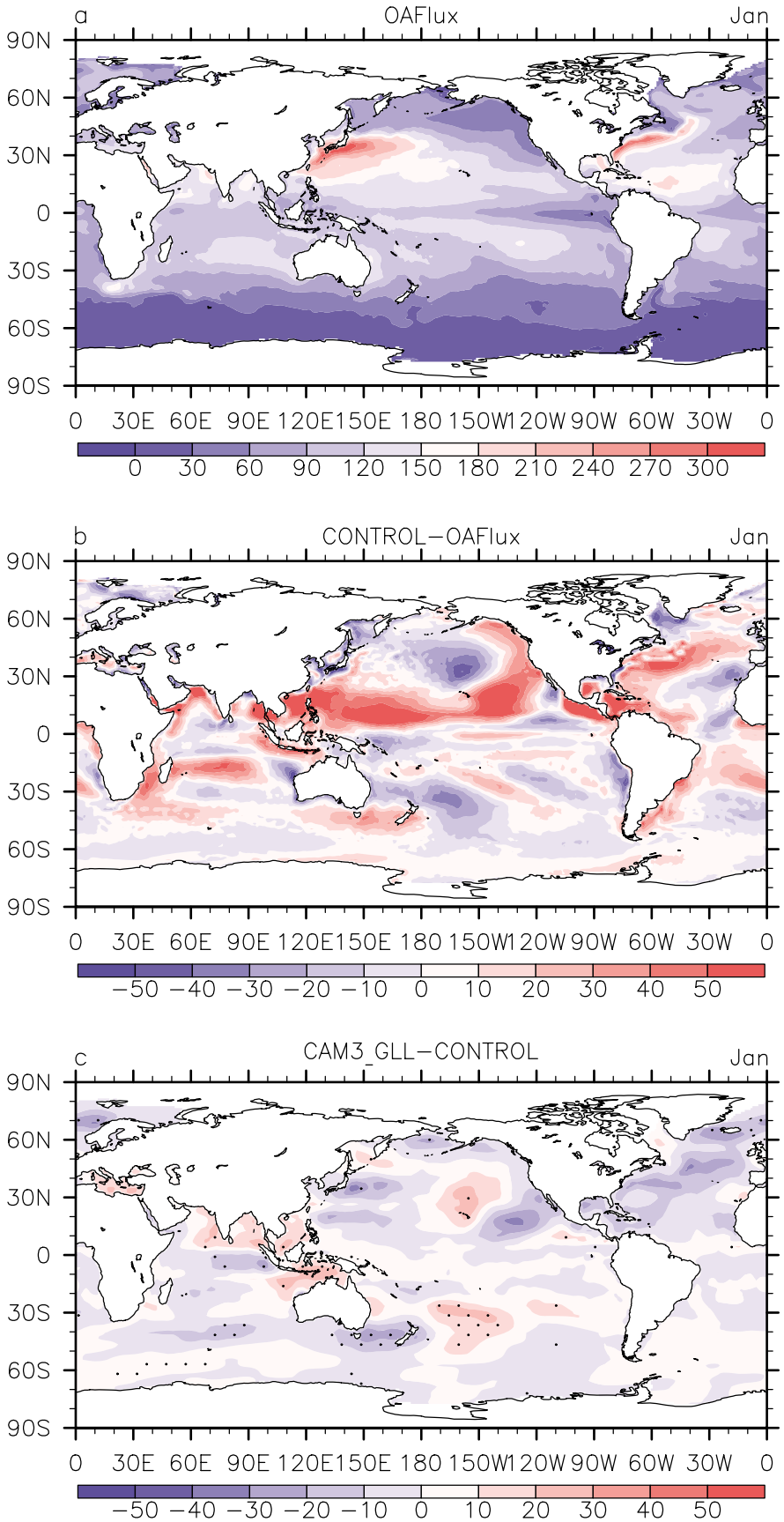

Figure 9. Surface latent heat flux (in W m^{-2}) in January. (a) OAFlux (1958–2006), (b) the difference between the control run and OAFlux, and (c) the difference between CAM3_GLL and the control run. Shaded areas show significant change at the 95% level, estimated by a Student's *t* test.

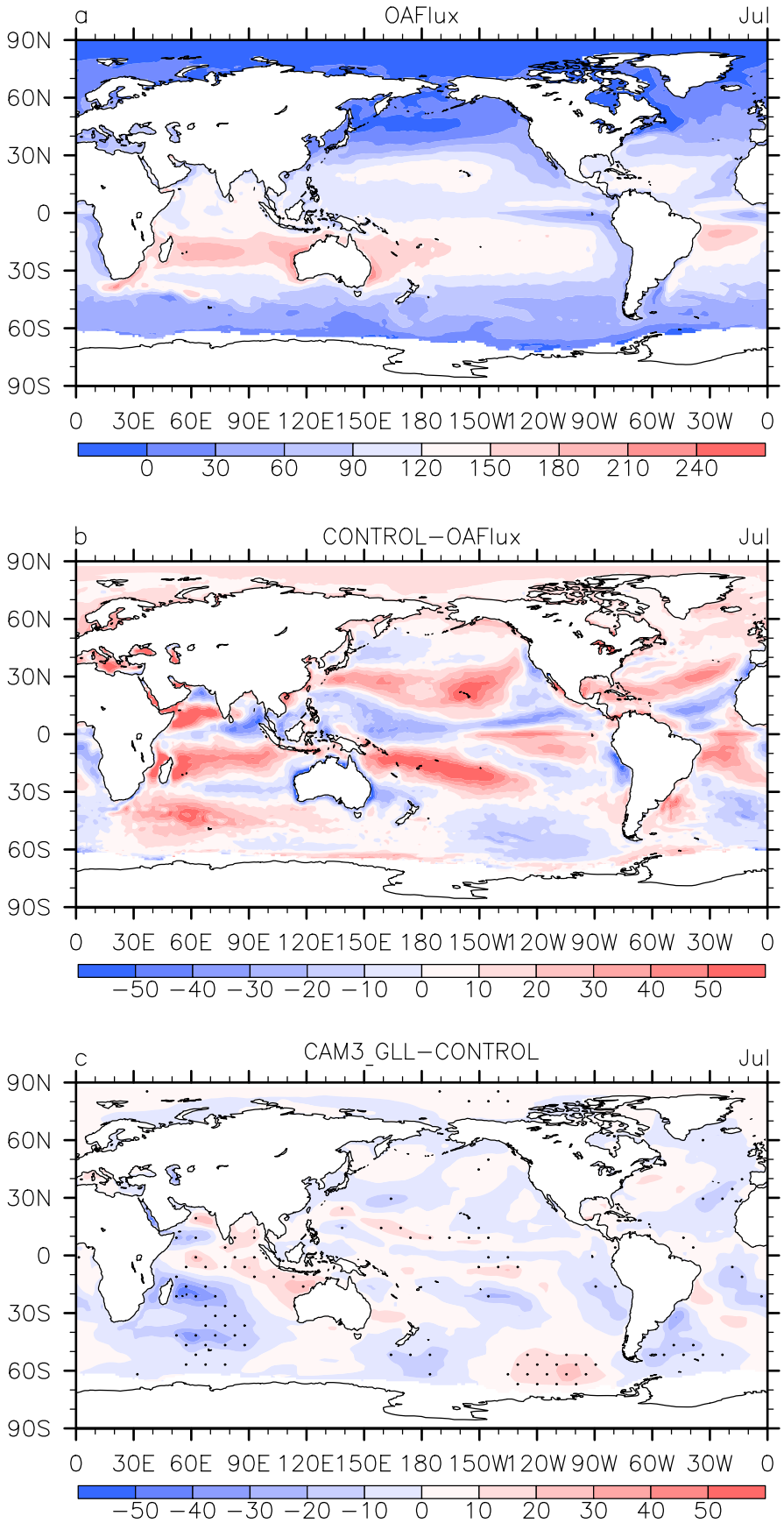

Figure 10. Same as Figure 9 but for July.

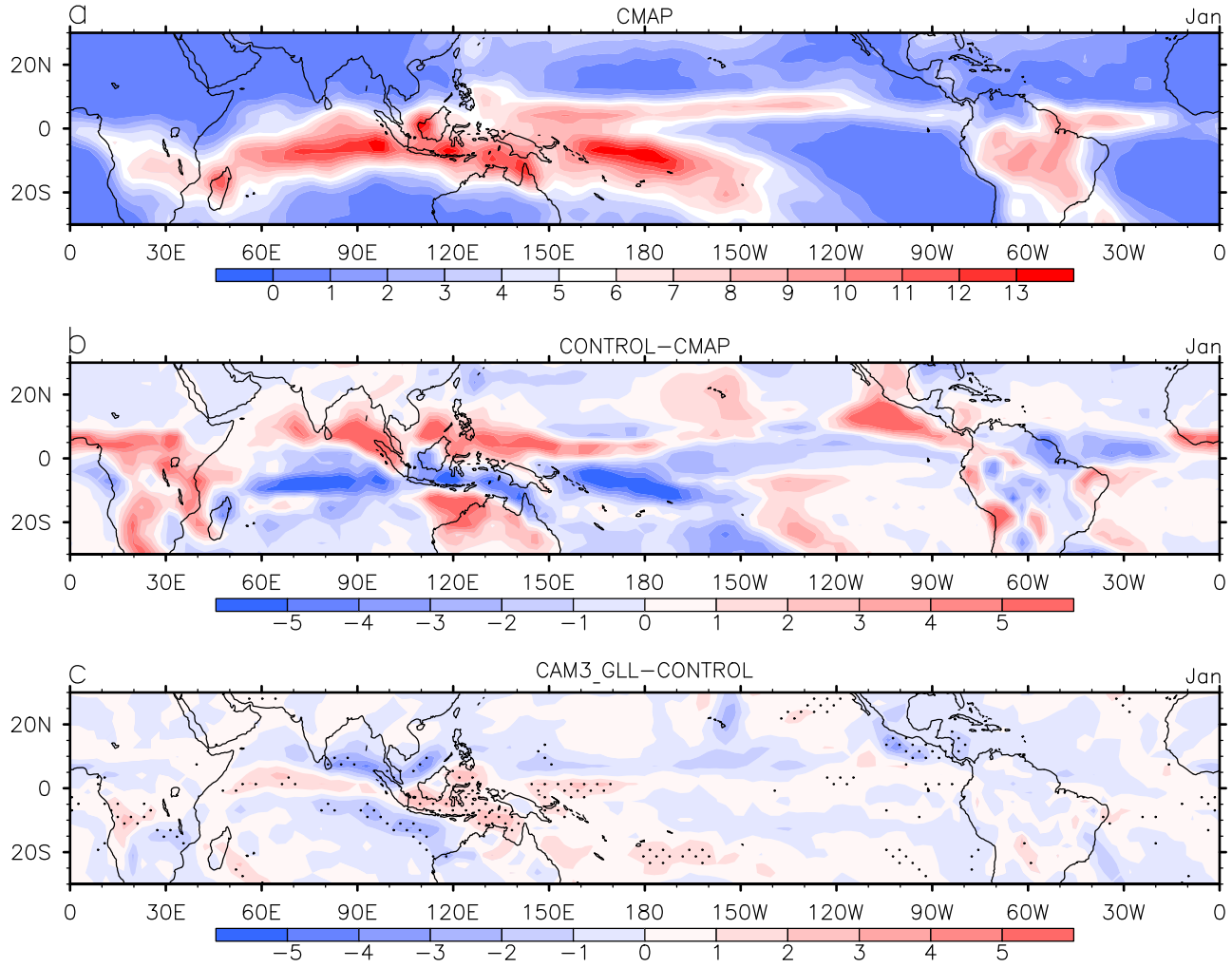

Figure 11. Precipitation (in mm d^{-1}) in January. (a) CMAP (1979–1998), (b) the difference between the control run and CMAP, and (c) the difference between CAM3_GLL and the control run. Shaded areas show significant change at the 95% level, estimated by a Student's *t*-test.

3.2.3. Sensible Heat Flux

[25] Figure 8 shows surface sensible heat flux over the Northern Hemisphere in January. A positive flux represents a transfer of heat from ocean to atmosphere. During boreal winter, over the North Atlantic Ocean, large sensible heat flux with OAFlux occurs in the Gulf Stream and its extensions over the Labrador and Norwegian Seas (Figure 8a); over the North Pacific Ocean, the elevated sensible heat fluxes occur over the Kuroshio, the Sea of Japan, the Sea of Okhotsk, and the Bering Sea (Figure 8a). In the Sea of Okhotsk and Labrador Sea, the differences between the control run and OAFlux exceeds 25 W m^{-2} (Figure 8b), and there is a statistically significant (at the 95% level) decrease in the bias in this region in the CAM3_GLL run (Figure 8c).

3.2.4. Latent Heat Flux

[26] Figures 9 and 10 show latent heat flux estimated from OAFlux, the difference between control and OAflux, and the difference between CAM3_GLL and control, respectively, in January and July. During boreal winter, large latent heat flux with OAFlux (Figure 9a) is seen in the western boundary warm current regions of the Kuroshio, the Gulf Stream, and their extensions, where the sensible heat flux is also large in these regions. Observational studies have shown these fluxes to be the largest during cold-air outbreaks, when a cold and dry air mass from the continent is advected over the relatively warm ocean [*Agee and Howley*, 1977; *Blanton et al.*, 1989; *Grossman and Betts*, 1990; *Xue et al.*, 1995]. This is due to high surface winds coupled with large sea-air humidity differences. Small latent heat flux is seen in the eastern equatorial Pacific and Atlantic due to weak winds and upwelling-induced low sea surface temperature. In the equatorial eastern Indian Ocean–western Pacific warm pool region, the latent heat flux is also small, which is mainly due to weak surface winds. During southern winter, large latent heat flux appears over such boundary current regions as the Agulhas Current off the African coast, the Falkland-Brazilian Current off of South America, and the Eastern Australian Current (Figure 10a). The flux intensification over these boundary current regions during the Southern Hemispheric wintertime is not as strong as their Northern Hemispheric counterparts. *Yu and Weller* [2007] pointed out that this is perhaps due to the fact that the continental landmasses of the Southern Ocean not only terminate in the subtropics,

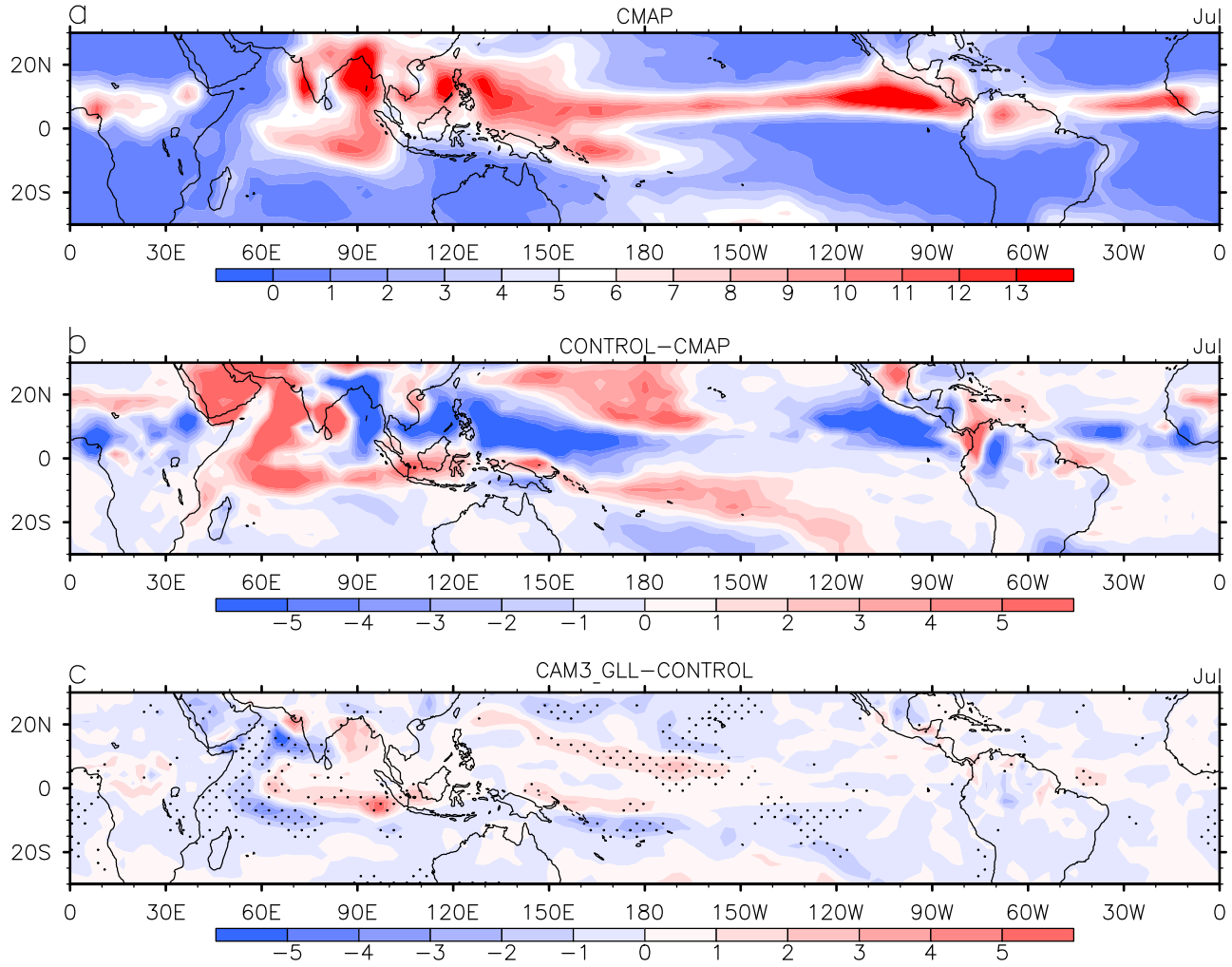

Figure 12. Same as Figure 11 but for July.

but also are relatively narrow, so the air masses advected over the currents are warmer and drier.

[27] The spatial distributions of latent heat flux in the control run and CAM3_GLL in January and July are similar to those of OAFlux. However, there are quantitative differences among them. Generally, the biases near boundary regions between the OAFlux and control run are associated with ocean currents; i.e., positive biases occur in the warm current region, such as in the Alaska, Gulf Stream, Brazil, Agulhas, and Mozambique warm currents, while negative biases occur in cold current regions, such as the Oyashio, California, Benguela, Peru, and West Australia cold currents. Over the Gulf Stream, the control run produces much larger latent heat flux than that observed; the difference in these regions exceeds 30 W m^{-2} (Figure 9b), and CAM3_GLL reduces the biases by 15–20 W m^{-2}, which is close to OAFlux. Over the open oceans, such as in the subtropical trade wind regions, the surface evaporation in the control run is higher than that observed (Figure 9b), This is also the case in CCM3 [*Kiehl et al.*, 1998; *Zhang et al.*, 1998] due to the stronger trade winds associated with the stronger subtropical surface high-pressure centers compared to the observations [*Hurrell et al.*, 1998]. The latent heat flux is rectified in CAM3_GLL in this region. In July, the control run produces large biases over the Arabian Sea and the Bay of Bengal region (absolute value exceeds ~40 W m^{-2}) (Figure 10b), and the biases are reduced in CAM3_GLL (Figure 10c).

3.2.5. Precipitation

[28] The horizontal distribution of January and July averaged precipitation (CMAP), the difference between the control run and CMAP, and the difference between CAM3_GLL and the control run are shown in Figures 11 and 12, respectively. Although the CAM3 simulation captures many of the observed features in the global precipitation distribution, it continues to share many of the same biases exhibited by CCM3. CAM3_GLL reduces the biases in some regions. For example, in the boreal winter, the control run produces too much precipitation over the Arabian Sea, the Bay of Bengal, and South China Sea, as pointed out by *Hurrell et al.* [2006], and the GLL parameterization reduced the above-mentioned biases by 0.5–1.5 mm d^{-1} as seen in Figure 11c. In boreal summer, the most serious simulation errors in the control run (Figure 12b) occur over the northern Indian Ocean, the Arabian Sea, and the Arabian Peninsula, all of which have increased precipitation by more than 4 mm d^{-1}, while CAM3_GLL decreases by 1–2 mm d^{-1} in this region compared to the original parameterization as seen in Figure 12c. In sharp contrast, a low precipitation rate occurs

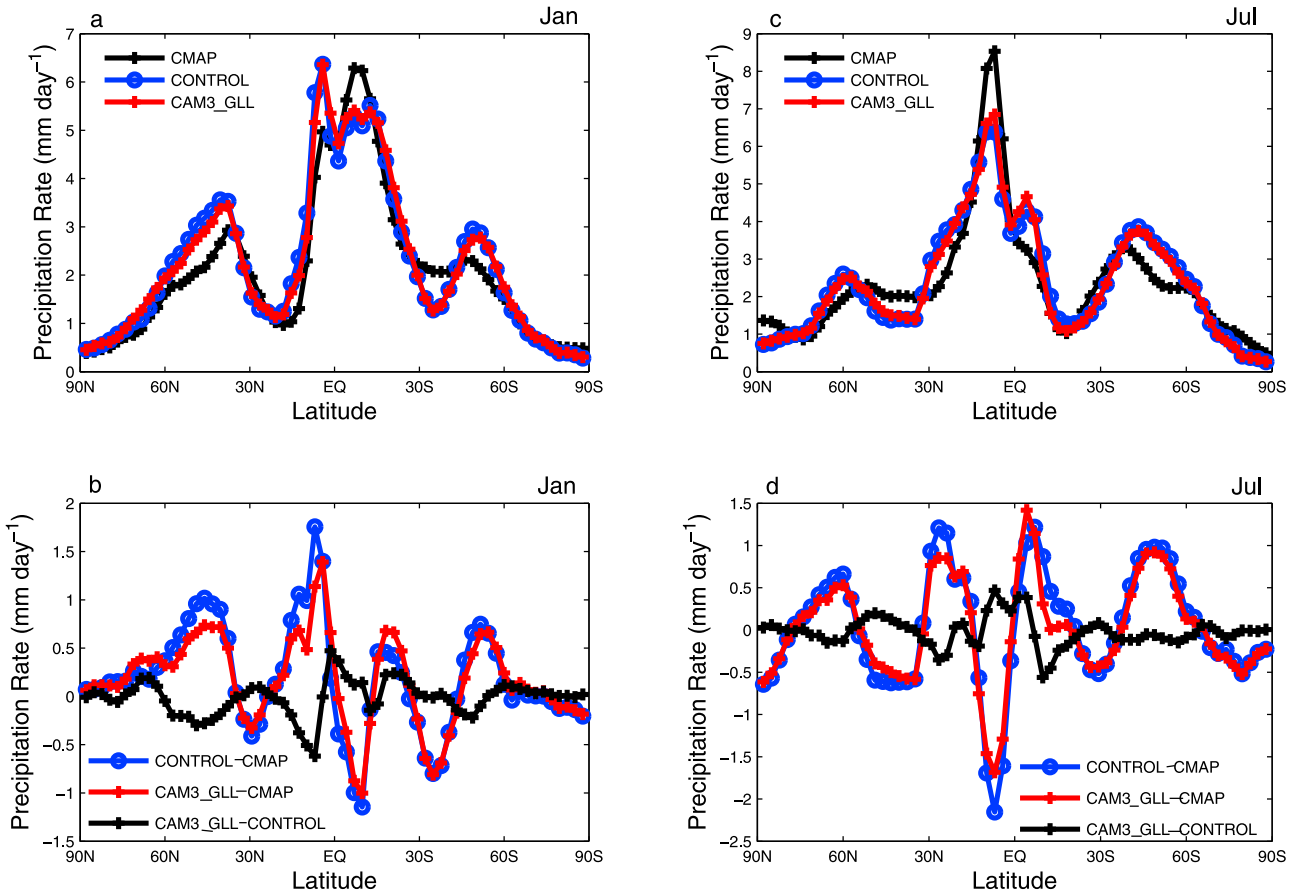

Figure 13. (a) Zonal average of precipitation in January, (b) zonal average difference among the control run, CAM3_GLL, and CMAP in January, and (c and d) same as Figures 13a and 13b, respectively, but for July.

in the control run from the South China Sea through the Philippine Sea, into the tropical equatorial Pacific, as well as the eastern Bay of Bengal. This precipitation pattern is represented as a relatively diffuse extension of the Southeast Asian monsoon well into the central Pacific subtropics, and is a long-standing precipitation bias in the CCM and CAM models [*Hack et al.*, 2006]. These biases have been decreased by 0.5 mm d^{-1} to 2 mm d^{-1} in CAM3_GLL. *Brunke et al.* [2008] also partially improved the predicted precipitation in this region by incorporating a prognostic skin sea surface temperature algorithm [*Zeng and Beljaars*, 2005] into CAM3.

[29] The zonally averaged distribution of precipitation for the control and CAM3_GLL runs in January is shown in Figure 13a, in comparison with precipitation estimates from CMAP. There is a tendency for the simulated tropical precipitation maxima to remain in the Northern Hemisphere throughout the year, while most observation data sets show a clear seasonal migration of Intertropical Convergence Zone (ITCZ) precipitation across the equator, as reported by *Hack et al.* [2006], *Hurrell et al.* [2006], and *Collins et al.* [2006a, 2006b]. The CAM3_GLL run reduces the Northern Hemisphere tropical precipitation of the control run by 0.2–0.4 mm d^{-1}. The Northern Hemisphere secondary maxima precipitation biases were also reduced by about 0.3 mm d^{-1} as seen in Figure 13b. Figures 13c and 13d show zonal average of precipitation and zonal average difference among the control, CAM3_GLL, and CMAP runs in July. CAM3_GLL increased the Northern Hemisphere tropical precipitation and decreased the secondary maximum precipitation, and the zonal average precipitation simulated by CAM3_GLL is closer to CMAP.

4. Conclusions

[30] This study examines the response of the climate simulation by the NCAR CAM3 to the air-sea turbulent flux scheme. The major difference between the GLL scheme and the CAM3 air-sea turbulent flux scheme is that the former gives a new expression for the transfer coefficients and a greater computational efficiency. The stability functions for stable and unstable stratification were adjusted to those of *Beljaars and Holtslag* [1991] and *Högström* [1996], respectively. The CAM3 requires iterative solutions to bulk flux equations, which utilize the stability functions of *Dyer* [1974]. The offline test using TOGA COARE data shows that the GLL scheme improved the CAM3 results especially under very weak winds. The CAM3 evaluation shows that the GLL scheme produces more realistic surface wind stress in the North Pacific and North Atlantic trade wind belts and wintertime extratropical storm track regions. The latent heat flux in the Northern Hemisphere trade wind zones shows modest improvement in the GLL scheme, and the latent heat flux bias in the western boundary current region of the Gulf

Stream is reduced. In addition, the simulated precipitation in the GLL scheme is closer to the observations in the Asia monsoon region.

[31] **Acknowledgments.** This study was mainly supported by MOST (2006CB403600, 2006CB400500, 2006BAB18B03, 2006BAB18B05, 2008BAC40B05, and 2010CB428502), by CMA (GYHY(QX)2007-6-5), by NSFC (40975009 and 40906023), and by the Centurial Program sponsored by the Chinese Academy of Sciences (CAS). The National Center for Atmospheric Research is sponsored by the National Science Foundation. We are very grateful to three anonymous reviewers for their careful review and valuable comments, which led to substantial improvement of this manuscript.

References

Agee, E. M., and R. P. Howley (1977), Latent and sensible heat flux calculations at the air-sea interface during AMTEX 74, *J. Appl. Meteorol.*, *16*, 443–447.

Alexander, M., J. Yin, G. Branstator, A. Capotondi, C. Cassou, R. Cullather, Y.-O. Kwon, J. Norris, J. Scott, and I. Wainer (2006), Extratropical atmosphere-ocean variability in CCSM3, *J. Clim.*, *19*, 2492–2521.

Beljaars, A. C., and A. A. M. Holtslag (1991), Flux parameterization over land surfaces for atmospheric models, *J. Appl. Meteorol.*, *30*, 327–341.

Blanton, J. O., J. A. Amft, D. K. Lee, and A. Riordan (1989), Wind stress and heat fluxes observed during winter and spring 1986, *J. Geophys. Res.*, *94*, 10,686–10,698.

Bonan, G. B., K. W. Oleson, M. Vertenstein, S. Levis, X. Zeng, Y. Dai, R. E. Dickinson, and Z-L. Yang (2002), The land surface climatology of the Community Land Model coupled to the NCAR Community Climate Model, *J. Clim.*, *15*, 3123–3149.

Brunke, M. A., X. Zeng, and S. Anderson (2002), Uncertainties in sea surface turbulent flux algorithms and data sets, *J. Geophys. Res.*, *107*(C10), 3141, doi:10.1029/2001JC000992.

Brunke, M. A., C. W. Fairall, X. Zeng, L. Eymard, and J. A. Curry (2003), Which bulk aerodynamic algorithms are least problematic in computing ocean surface turbulent fluxes?, *J. Clim.*, *16*, 619–635.

Brunke, M. A., X. Zeng, W. Misra, and A. Beljaars (2008), Integration of a prognostic sea surface skin temperature scheme into weather and climate models, *J. Geophys. Res.*, *113*, D21117, doi:10.1029/2008JD010607.

Byun, D. W. (1990), On the analytical solutions of flux-profile relationships for the atmospheric surface layer, *J. Appl. Meteorol.*, *29*, 652–657.

Capps, S. B., and C. S. Zender (2008), Observed and CAM3 GCM sea surface wind speed distributions: Characterization, comparison, and bias reduction, *J. Clim.*, *21*, 6569–6585.

Collins, W. D., et al. (2004), Description of the NCAR Community Atmosphere Model (CAM3), *Tech. Rep. NCAR/TN- 464_STR*, 226 pp., Nat. Cent. for Atmos. Res., Boulder, Colo.

Collins, W. D., et al. (2006a), The Community Climate System Model version 3 (CCSM3), *J. Clim.*, *19*, 2122–2143.

Collins, W. D., P. J. Rasch, B. A. Boville, J. J. Hack, J. R. McCaa, D. L. Williamson, B. P. Briegleb, C. M. Bitz, S.-J. Lin, and M. H. Zhang (2006b), The formulation and atmospheric simulation of the Community Atmosphere Model: CAM3, *J. Clim.*, *19*, 2144–2161.

Dyer, A. J. (1974), A review of flux-profile relationships, *Boundary Layer Meteorol.*, *7*, 363–372.

Fairall, C. W., E. F. Bradley, D. P. Rogers, J. B. Edson, and G. S. Young (1996), Bulk parameterization of air-sea fluxes for Tropical Ocean–Global Atmosphere Coupled-Ocean Atmosphere Response Experiment, *J. Geophys. Res.*, *101*(C2), 3747–3764.

Fairall, C. W., A. B. White, J. B. Edson, and J. Hare (1997), Integrated shipboard measurements of the marine boundary layer, *J. Atmos. Oceanic Technol.*, *14*, 338–359.

Fairall, C. W., E. F. Bradley, J. E. Hare, A. A. Grachev, and J. B. Edson (2003), Bulk parameterization of air-sea fluxes: Updates and verification for the COARE algorithm, *J. Clim.*, *16*, 571–591.

Grachev, A. A., and C. W. Fairall (1997), Dependence of the Monin-Obukhov stability parameter on the bulk Richardson number over the ocean, *J. Appl. Meteorol.*, *36*, 406–414.

Grossman, R. L., and A. K. Betts (1990), Air-sea interaction during an extreme cold air outbreak from the eastern coast of the United States, *Mon. Weather Rev.*, *118*, 324–342.

Hack, J. J., J. M. Caron, G. Danabasoglu, K. W. Oleson, C. M. Bitz, and J. E. Truesdale (2006), CCSM-CAM3 climate simulation sensitivity to changes in horizontal resolution, *J. Clim.*, *19*, 2267–2289.

Högström, U. (1996), Review of some basic characteristics of the atmospheric surface layer, *Boundary Layer Meteorol.*, *78*, 215–246.

Hurrell, J. W., J. J. Hack, B. A. Boville, D. L. Williamson, and J. T. Kiehl (1998), The dynamical simulation of the NCAR Community Climate Model version 3 (CCM3), *J. Clim.*, *11*, 1207–1236.

Hurrell, J. W., J. J. Hack, A. S. Phillips, J. Caron, and J. Yin (2006), The dynamical simulation of the Community Atmosphere Model Version 3 (CAM3), *J. Clim.*, *19*, 2162–2183.

Kiehl, J. T., J. J. Hack, and J. W. Hurrell (1998), The energy budget of the NCAR Community Climate Model: CCM3, *J. Clim.*, *11*, 1151–1178.

Large, W. G., and S. Pond (1982), Sensible and latent heat flux measurements over the oceans, *J. Phys. Oceanogr.*, *12*, 464–482.

Large, W. G., J. C. McWilliams, and S. C. Doney (1994), Oceanic vertical mixing: A review and a model with a nonlocal boundary layer parameterization, *Rev. Geophys.*, *32*, 363–403.

Launiainen, J. (1995), Derivation of the relationship between the Obukhov stability parameter and the bulk Richardson number for flux-profile studies, *Boundary Layer Meteorol.*, *76*, 165–179.

Lee, H. N. (1997), Improvement of surface flux calculations in the atmospheric surface layer, *J. Appl. Meteorol.*, *36*, 1416–1423.

Liu, W. T., K. B. Katsaros, and J. A. Businger (1979), Bulk parameterization of the air-sea exchange of heat and water vapor including the molecular constraints at the interface, *J. Atmos. Sci.*, *36*, 2052–2062.

Louis, J. F. (1979), A parametric model of vertical eddy fluxes in the atmosphere, *Boundary Layer Meteorol.*, *17*, 187–202.

Louis, J. F., M. Tiedtke, and J. F. Geleyn (1982), A short history of the operational PBL-parameterization at ECMWF, paper presented at Workshop on Planetary Boundary Layer Parameterization, Eur. Cent. for Medium-Range Weather Forecasts, Reading, U. K.

Oleson, K. W., Y. Dai, G. B. Bonan, and M. Bosilovich (2004), Technical description of the Community Land Model (CLM), *Tech. Rep. NCAR/TN-461_STR*, 174 pp., Natl. Cent. for Atmos. Res., Boulder, Colo.

Pielke, R. A., et al. (1992), A comprehensive meteorological modeling system—RAMS, *Meteorol. Atmos. Phys.*, *49*, 69–91.

Rasch, P. J., M. J. Stevens, L. Ricciardulli, A. Dao, A. Negri, R. Wood, B. A. Boville, B. Eaton, and J. J. Hack (2006), Characterization of tropical transient activity in the CAM3 atmospheric hydrologic cycle, *J. Clim.*, *19*, 2222–2242.

Trenberth, K. E. (1990), Recent observed interdecadal climate changes in the Northern Hemisphere, *Bull. Am. Meteorol. Soc.*, *71*, 988–993.

Urlikson, B., and C. F. Mass (1990), Numerical investigation of mesoscale circulations over the Los Angeles Basin, Part I, A verification study, *Mon. Weather Rev.*, *118*, 2138–2161.

Wang, S., Q. Wang, and J. Doyle (2002), Some improvements to Louis surface flux parameterization, paper presented at 15th Symposium on Boundary Layers and Turbulence, Am. Meteorol. Soc., Wageningen, Netherlands.

Xie, P., and P. A. Arkin (1997), Analyses of global monthly precipitation using gauge observations, satellite estimates, and numerical model predictions, *J. Clim.*, *9*, 840–858.

Xue, H., J. M. Bane Jr., and L. M. Goodman (1995), Modification of the Gulf Stream through strong air-sea interaction in winter: Observations and numerical simulations, *J. Phys. Oceanogr.*, *25*, 533–557.

Yu, L., and R. A. Weller (2007), Objectively analyzed air-sea heat fluxes for the global ice-free oceans (1981–2005), *Bull. Am. Meteorol. Soc.*, *88*, 527–539.

Yu, L., R. A. Weller, and B. Sun (2004), Improving latent and sensible heat flux estimates for the Atlantic Ocean (1988–99) by a synthesis approach, *J. Clim.*, *17*, 373–393.

Zeng, X., and A. Beljaars (2005), A prognostic scheme of sea surface skin temperature for modeling and data assimilation, *Geophys. Res. Lett.*, *32*, L14605, doi:10.1029/2005GL023030.

Zeng, X., M. Zhao, and R. E. Dickinson (1998), Intercomparison of bulk aerodynamic algorithms for the computation of sea surface fluxes using TOGA COARE and TAO data, *J. Clim.*, *11*, 2628–2644.

Zhang, G. J., J. T. Kiehl, and P. J. Rasch (1998), Response of climate simulation to a new convective parameterization in the National Center for Atmospheric Research Community Climate Model (CCM3), *J. Clim.*, *11*, 2097–2115.

J. Ban and Z. Gao, State Key Laboratory of Atmospheric Boundary Layer Physics and Atmospheric Chemistry, Institute of Atmospheric Physics, Chinese Academy of Sciences, Box 9804, Beijing 100029, China. (zgao@mail.iap.ac.cn)

D. H. Lenschow, National Center for Atmospheric Research, Boulder, CO 80307, USA.